Compact Self-Packaged Dual-Band Filter Using Multilayer Liquid Crystal Polymer Technology

Francisco J. Cervera, *Member, IEEE*, and Jiasheng Hong, *Fellow, IEEE*

***Abstract*—A compact self-packaged dual-band filter structure using multilayer liquid crystal polymer technology is presented in this paper. The frequency and bandwidth of each passband can be more conveniently controlled by means of vertically embedded elements, i.e., metal patches, placed above the coupled folded multi-stepped impedance resonators. The packaged solution is connected to the outer environment through a coplanar waveguide that allows flip-chip interconnection to a host board. The proposed design is validated with the fabrication of two prototypes. The measured results show good agreement with the simulations.**

***Index Terms*—Dual-band filters, liquid crystal polymer (LCP), microwave filters, self-packaged filters.**

I. Introduction

As wireless communications penetrate more and more in our daily lives, different systems and transmission technologies have to be developed to fit them properly. Mobile phones or laptops, as an example, often integrate technologies like WiFi, Bluetooth, GSM, or GPS. Each of these services has receivers/transmitters operating in different frequencies that have to be accommodated in a small, portable device. Multiband radio frontends are often employed for this matter, and, here, multiband filters play a key role.

Extensive work has been carried recently in the field of dual-band filters [1]–[16], and different approaches on how to produce the passbands have been reported. The most common approach is to employ multimode resonators and locate the passbands at the resonant frequencies [2], [3], [5]–[7], [11], [12]. The resonant modes are split by means of inter-resonator coupling in order to control the bandwidth. The separation between the bands depends on the modes of the resonator, placing some design constraints. Alternatively, in [10], only one ring resonator is used to produce the two passbands. In this case the split of each resonant mode is obtained by a pair of open-circuited stubs attached to the resonator. Even though it has the advantage of using only one resonator, it also has the limitations of a small frequency ratio between the passbands. In the other hand, the use of four resonators is reported in [8], [9].

Manuscript received April 10, 2014; revised July 03, 2014; accepted September 01, 2014. Date of publication October 09, 2014; date of current version November 03, 2014. This work was supported in part by the U.K. EPSRC Industrial CASE Award in association with BSC Filters Ltd., U.K.

The authors are with the Department of Electrical, Electronic and Computer Engineering, School of Engineering and Physical Sciences, Heriot-Watt University, Edinburgh, EH14 4AS, U.K. (e-mail: fc88@hw.ac.uk; J.Hong@hw.ac.uk).

Color versions of one or more of the figures in this paper are available online at http://ieeexplore.ieee.org.

Digital Object Identifier 10.1109/TMTT.2014.2359635

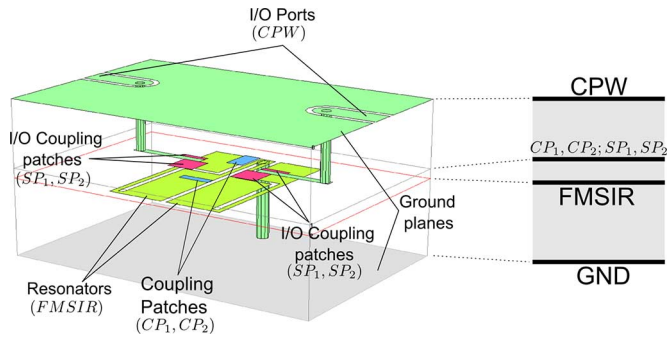

Fig. 1. Proposed self-packaged dual-band filter multilayer structure.

Additionally, methods for producing each band independently, combining two bandpass filters, have been covered in[4], [14]. Finally, a method based on successive transformations from a lowpass prototype is presented in [1], and a semi-lumped element approach cascading several bandpass cells in reported in [13]. These methods simplify the design process usually at the cost of increased footprint.

The multilayer structure proposed in this work (Fig. 1) consists of four metal layers. On the central layer, two coupled dual-mode resonators are placed next to each other in a mirrored disposition. The coupling between them is produced first by this proximity between them and, second, by a pair of metal patches $(\mathrm{CP}_1, \mathrm{CP}_2)$, placed on the layer above them, that controls the coupling coefficients for each of the passbands. Finally, the coupling between the resonators and the input/output ports is achieved by a second pair of patches $(\mathrm{SP}_1, \mathrm{SP}_2)$ whose area determines the external quality factor (Q_e) for each band. The top and bottom layers are the ground planes, also providing electromagnetic shielding to the filter. Furthermore, the top layer contains a pair of coplanar waveguide (CPW) lines that connect the filter to the external environment through a vertical via transition. The whole packaged filter is implemented using liquid crystal polymer (LCP) material.

The remainder of this paper is structured as follows. In Section II, the critical design parameters of the proposed filter are described and analyzed. Section III explains the design process of the discussed dual-band filter, following two design examples and the results after fabrication in Section IV. Finally, conclusions are presented in Section V.

II. Design Analysis

A. Dual-Mode Resonator

The essential resonator deployed in the dual-band filter design can be seen as a folded multi-stepped impedance resonator (FMSIR) with four sections alternating high and low

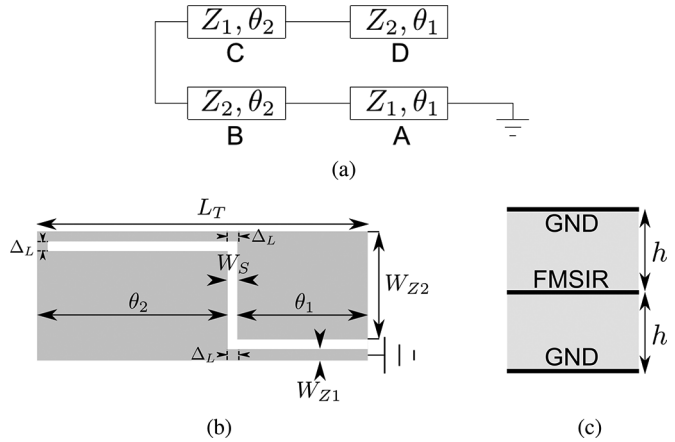

Fig. 2. Proposed FMSIR structure. (a) Transmission-line model. Letters A-D denote individual line sections. (b) Physical realization. (c) Layer distribution.

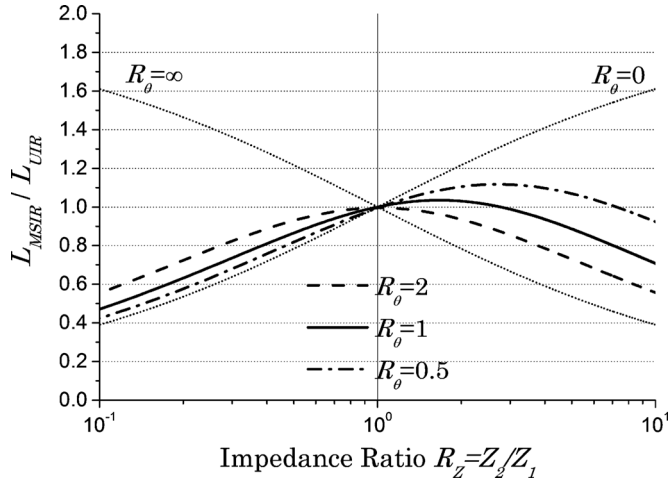

Fig. 3. Length of the unfolded resonator (L_{MSIR}) compared with the length of a conventional UIR (L_{UIR}) for different values of R_θ and R_Z. This is qquivalent to the ratio between fundamental resonant frequencies when both lengths are equal.

impedance, with one end open-circuited and the other end short-circuited, as a quarter-wavelength resonator [Fig. 2(a)]. This alternating structure allows for a compact layout when folding two sections over the other two [as depicted in Fig. 2(b)] by adding extra length to some of the sections (Δ_L).

Spurious coupling is expected when folding the resonator in such a manner between adjacent lines, as it is stronger where the current density is higher and the distance between them smaller. However, at FMSIR resonant frequencies, most of the current density is accumulated at the high-impedance sections, which are always next to a low-impedance section, with low current density [cf. (8)]. This property makes the coupling between adjacent lines negligible, avoiding significant interaction even if the gap between the lines is small. Hence, the width of the slotline (W_S) can be reduced down to fabrication tolerances without having a direct impact on the resonant frequencies. Variations to the resonant frequencies respect to the ideal model [Fig. 2(a)] are mainly due to the length of the Δ_L sections [Fig. 2(b)] and larger as this length increases. Since Δ_L is directly related to W_S, it is desirable to design them to be as small as possible.

Conventional quarter-wavelength resonators with uniform impedance (UIR) resonate at integer odd multiples of the fundamental frequency (f_0), i.e., $(2n+1)f_0$ with $n = 1, 2, 3\ldots$ It is well known that a quarter-wavelength SIR (single step) is able to shift the first harmonic frequency (f_1) away from $3f_0$ depending on the impedance ratio (R_Z) of its two sections [17]. In this study, it will be demonstrated how the FMSIR enhances this property by offering more control over the positioning of the second harmonic (f_2).

Ignoring the effects of the step discontinuities and the increased lengths of the sections (Δ_L) with Z_1, the input impedance (Z_{in}), looking into the open end of the resonator, can be determined as

$$Z_{\mathrm{in}} = \frac{jZ_1R_Z}{\Delta}R_Z(1+R_Z)(\tan\theta_1+\tan\theta_2-\tan^2\theta_1\tan\theta_2) - \frac{jZ_1R_Z}{\Delta}(1+R_Z^3)\tan\theta_1\tan^2\theta_2$$
$$\Delta = R_Z^2 - 2R_Z(1+R_Z)\tan\theta_1\tan\theta_2 - R_Z\tan^2\theta_1 - R_Z^3\tan^2\theta_2 + \tan^2\theta_1\tan^2\theta \quad (1)$$

where $R_Z = Z_2/Z_1$ is the impedance ratio between the lines. From (1), the resonance condition is described as

$$R_Z^2 - 2R_Z(1+R_Z)\tan\theta_1\tan\theta_2 - R_Z\tan^2\theta_1 - R_Z^3\tan^2\theta_2 + \tan^2\theta_1\tan^2\theta_2 = 0. \quad (2)$$

By defining the line length ratio as $R_\theta = \theta_2/\theta_1$, the resonator's behavior can be fully determined according to R_Z, R_θ, and the total electrical length of the resonator described in terms of its total electrical length (θ_T) as follows:

$$\theta_T = 2(\theta_1+\theta_2). \quad (3)$$

For comparison, the normalized length (L_n) of the unfolded resonator (L_{MSIR}) with respect of that of a conventional UIR (L_{UIR}) is defined as

$$L_n = \frac{\theta_T}{\pi/2}. \quad (4)$$

Fig. 3 shows L_n for several combinations of R_Z and R_θ. Note that, when $R_Z = 1$, the FMSIR becomes an UIR and the lengths are equal. Also, special cases are $R_\theta = \infty(\theta_1 = 0)$ and $R_\theta = 0(\theta_2 = 0)$, corresponding to single SIR with both sections equal in length and inverted R_Z.

For the purpose of designing a dual-band filter, the second passband will be determined by the frequency of the first-harmonic mode (f_1). In Fig. 4, it can be observed how f_1/f_0 can be controlled depending on the design parameters R_Z and R_θ. For $R_Z < 1$, the most determining parameter is R_θ, while for $R_Z > 1$ both R_Z and R_θ are equally relevant. Another conclusion from Fig. 4 is that, when $R_Z < 1$, the frequency variation is less sensitive to impedance variations, and this can be used as an advantage in the fabrication process, especially when dealing with etching tolerances.

Providing a wide stopband after the second passband is also a desirable property in a dual-band filter. This width is mainly determined by how far in frequency the second harmonic can

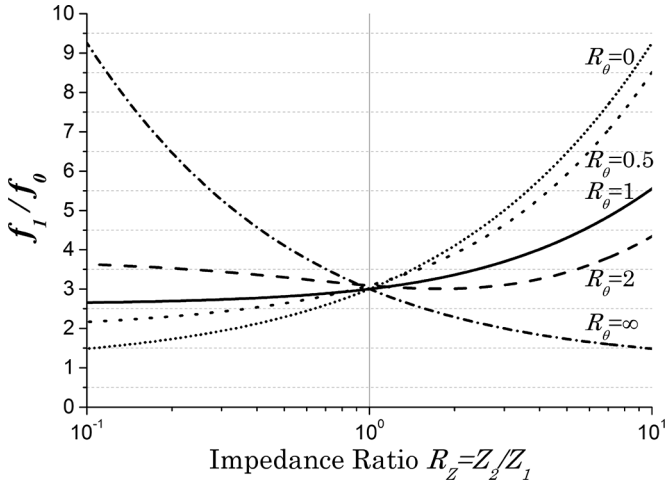

FIg. 4. Variations of first-harmonic frequency for different values of R_θ and R_Z.

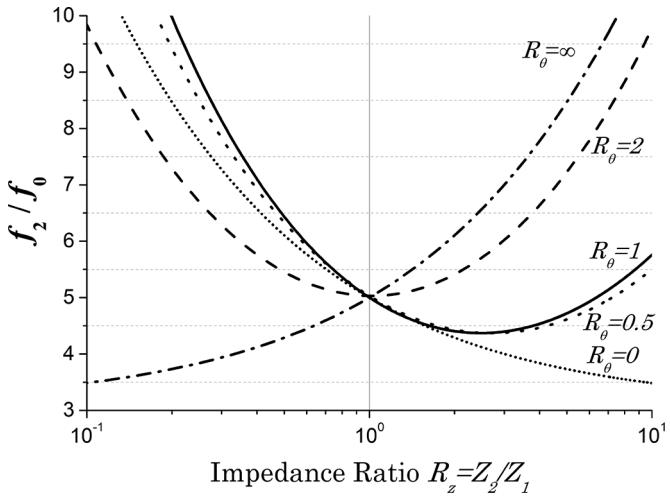

Fig. 5. Variations of second-harmonic frequency for different values of R_θ and R_Z.

be pushed away from the first harmonic. Fig. 5 shows that, for $R_Z < 1$, the maximum bandwidth is obtained for $R_\theta = 1$, while for $R_Z > 1$ the maximum is for $R_\theta = \infty$.

B. I/O Coupling

The resonator is coupled to the input/output ports through the capacitance created by two metal patches placed above the low-impedance sections of the resonator $(\mathrm{SP}_1, \mathrm{SP}_2)$ (Fig. 6). The amount of coupling is determined by the capacitance created between the metal patches, as a parallel-plates capacitor

$$C = \frac{\epsilon_0 \epsilon_r A}{h_c} \tag{5}$$

where $\epsilon_0 = 8.854 \times 10^{-12}$ F/m, ϵ_r is the relative dielectric constant of the substrate, A is the area of the parallel plates, and h_c is the separation between them. In this case, A is determined by the area of SP_1 or SP_2 and h_c by the thickness of the dielectric layer between the resonator and the I/O coupling layer. It is important to note that (5) is only valid for low frequencies.

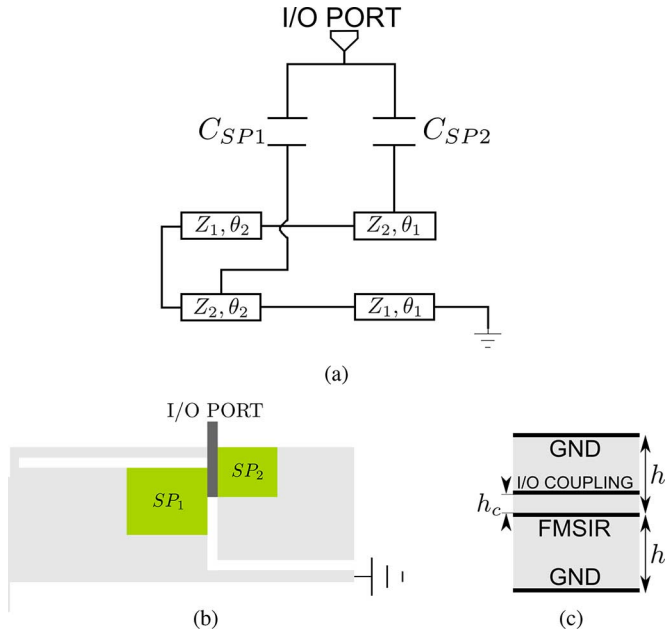

Fig. 6. I/O coupling. (a) Simplified transmission line model. Arrow shows the resonant section producing the in-band TZ. (b) Physical realization (top view) (c) Layer distribution.

The actual value of the capacitance created between the patches and the resonator will grow as frequency is increased until the capacitor's self-resonant frequency is reached. From that point, modelling the coupling as a pair of capacitors (C_SP1, C_SP2) is not possible.

In general, increasing the size of the patches will increase the coupling and hence reduce the external quality factor (Q_e). However, the variation of each patch will affect both bands, meaning that the value of the (Q_{e1}, Q_{e2}) set is a function of both coupling patches, i.e., SP_1 and SP_2 (cf. Figs. 11 and 15). Q_e is extracted using a technique described in [18].

When loading the FMSIR with C_SP1 and C_SP2, a shift of the resonant modes towards lower frequencies is expected. As the capacitance is increased, the loaded resonant modes approach those of the unloaded FMSIR.

C. Inter-Resonator Coupling

In order to produce the two desired passbands, proper couplings need to be facilitated. This is achieved by two different means: by the proximity of the resonators on the same layer and by two metal patches $(\mathrm{CP}_1, \mathrm{CP}_2)$ placed on the layer above the resonators along the symmetry plane. The individual equivalent patches for each resonator are joined together to form one single piece of metal [Fig. 7(b)].

The coupling coefficient (k) between the resonators may be electric (or capacitive) or magnetic (or inductive), being always a mix of both with one of them being dominant. To determine the k between two resonators, the circuit is analyzed by separately inserting a magnetic and an electric wall in the plane of symmetry. These two separate experiments provide two different resonant frequencies: f_e and f_m for electric and magnetic walls, respectively. From [19] and [20], it can be found that, if $f_e > f_m$, the coupling is predominantly magnetic and,

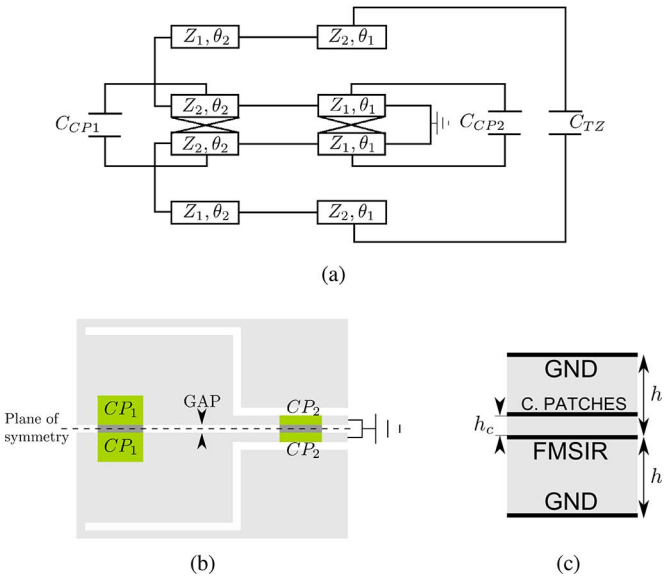

Fig. 7. Inter-resonator coupling. (a) Simplified transmission line model, including optional C_{TZ}. (b) Physical realization (top view) (c) Layer distribution.

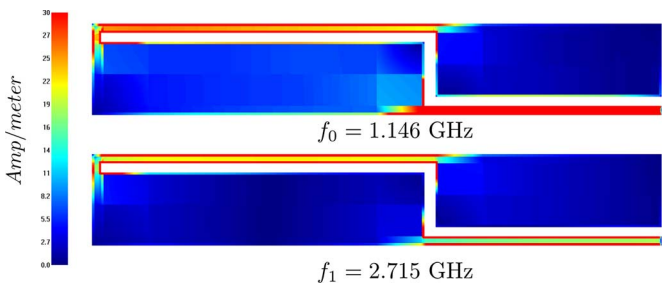

Fig. 8. Current density distribution for the first two resonant modes. $\epsilon_r = 3$, $h = 0.2$ mm. For the rest of the dimensions, see Fig. 13.

if $f_e < f_m$, it is predominantly electric. The effective k is calculated by

$$k = \frac{f_e^2 - f_m^2}{f_e^2 + f_m^2} \tag{6}$$

The coupling produced by the proximity of the resonators is predominantly magnetic and is stronger as the separation (GAP) is reduced. Fabrication tolerances place a limitation in the amount of coupling that can be obtained. Furthermore, by solely modifying the gap it is not possible to control k independently for each band.

Independent control over the coupling of each band separately (k_1, k_2) comes from the coupling patches CP_1 and CP_2. These two patches create the capacitances C_{CP1} and C_{CP2}, respectively [Fig. 7(a)] contributing to k_1 and k_2 differently. This property makes tuning k for each band possible. The type of coupling they produce is also different due to their positioning on the symmetry line. From Fig. 8, it is seen how the current density is higher in the high-impedance sections, and minimum at the other end of the symmetry line. Coupling between the high-density current sections contribute towards magnetic coupling, and low-density current sections, towards electric coupling. Hence, by placing CP_1 at the left end of the symmetry line it will be adding electric coupling, in different amount, to k_1 and k_2. As the position of CP_1 is shifted towards the other end, its contribution to the coupling progressively turns into magnetic. Similarly, from CP_2, the contribution is initially magnetic when placed at the rightmost of the symmetry line, turning into electric as shifted away from that point.

In general, the coupling will be stronger as their area of CP_1 and CP_2 is increased. However, since the effective k is a mix of both types of coupling, it could happen that they cancel each other when electric and magnetic coupling are equally strong. Getting the desired k_1 and k_2 is a combination of tuning GAP, areas of CP_1 and CP_2, and their position along the symmetry line.

D. Transmission Zeros (TZs) Mechanism of Generation

Several TZs are excited due to the different resonating modes of the FMSIR. A low-frequency TZ is generated by the resonance of the SIR formed by the transmission-line sections C and D [Fig. 2(a)]. This mode is excited when section B acts as a virtual connection to ground, making the aforementioned sections C and D behave as a $\lambda/4$ SIR. This mode will typically show between the two passbands. Moreover, a second resonant mode from this structure is also excited in the stopband. The frequencies for these modes can be calculated using the equations for SIR found in [17]. These two TZs are split into two pairs when inter-resonator coupling is put in place, and further control over them can be made by specifically coupling the sections C and D of both resonator. In this case, this is achieved by adding the capacitor C_{TZ} [Fig. 7(a)].

Depending on the position of the pair SP_1 and SP_2, two modes are excited. From the I/O patches looking into sections B and C, the resultant section behaves as an open-ended UIR with length θ_2. This section anti-resonates at odd multiples of $\lambda/4$. As previously discussed, the inter-resonator coupling is also able to split this TZ in two.

E. Packaging

Following the work carried in [21], the filter structure is enclosed within two ground planes in a stripline configuration. Additionally, a conductive paste is applied in the surrounding walls in order to achieve a full electromagnetic shielding.

The filter is connected the outer environment by means of a CPW, printed on one of the ground planes, and via transition (Fig. 1). This kind of packaging allows easy interconnection of the device to a hosting board in a flip-chip manner, as well as allowing easy matching of the input impedance by modifying the width and gap in the CPW.

III. Design Procedure

Due to the structure being so compact, the designs of resonator, I/O coupling and inter-resonator coupling are not really independent. Nevertheless, the design procedure described below can be useful.

First, depending on the substrate to be used, fix R_Z for the design. Then, depending on the required fundamental frequency, the length for a UIR is calculated using

$$L_{\mathrm{UIR}} = \frac{\lambda_g}{4} \approx \frac{1}{4}\frac{300}{f(\mathrm{GHz})\sqrt{\epsilon_r}}. \tag{7}$$

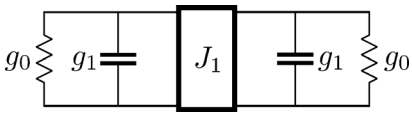

Fig. 9. Low-pass prototype filter.

Once L_{UIR} is computed, from Fig. 4 obtain the value for R_θ that matches the required f_1/f_0 ratio and R_Z. With this value, from Fig. 3 obtain the value for $L_{\mathrm{MSIR}}/L_{\mathrm{UIR}}$ to calculate the length of the MSIR, and physical length for θ_1 and θ_2, since R_θ is already known. Finally, L_T is calculated as $L_{\mathrm{MSIR}}/2$ plus W_S.

With the resonator tuned for f_0, the I/O patches have to be put in place for the required Q_e for each band. While tuning the I/O patches, the resonant frequencies will be affected and have to be retuned accordingly, as discussed in Section II-B.

Values for k and Q_e are calculated based on a low-pass, second-order Chebyshev prototype (Fig. 9) with normalized parameters $g_0 = 1.0$, $g_1 = 0.665$, $J_1 = 0.905$, and for a return loss of 20 dB. These parameters can be calculated by [18]

$$Q_{ei_1} = Q_{eo_1} = \frac{g_1}{\mathrm{FBW}_1}$$
$$Q_{ei_2} = Q_{eo_2} = \frac{g_1}{\mathrm{FBW}_2} \tag{8}$$
$$k_1 = \frac{\mathrm{FBW}_1 J_1}{g_1}$$
$$k_2 = \frac{\mathrm{FBW}_2 J_1}{g_1} \tag{9}$$

where Q_{ei_n} and Q_{eo_n} are the input and output external quality factors, k_n is the coupling coefficient, and FBW_n is the fractional ripple bandwidth. Index n represents the band. Even though calculations are intended for a single-band, they can be applied separately for each band, since both external quality factors and coupling coefficient is independently controlled for each band. Finally, inter-resonator coupling patches $(\mathrm{CP}_1, \mathrm{CP}_2)$ are included to provide the required coupling coefficient.

IV. Prototype Design and Results

In order to validate the previous analysis and parameter extraction, two prototypes are designed and fabricated following the same process. LCP substrate with the same layer distribution (Fig. 10) and fabrication technique is also applied for both designs.

For the given layer distribution and thickness of substrate (0.4 mm) the high and low impedance have a width of 0.2 and 1.6 mm, respectively, yielding 48 and 12 Ω ($R_Z = 0.25$). These dimensions are chosen bearing in mind etching tolerances and compactness, and so is W_S, which is fixed to 0.2 mm. To reduce the number of via holes required in the circuit, both resonators share the same grounding via [cf. Figs. 13(a) and 17(a)]. The patch for the ground via takes away some length from the line section A, producing some frequency shifting that needs to be compensated accordingly.

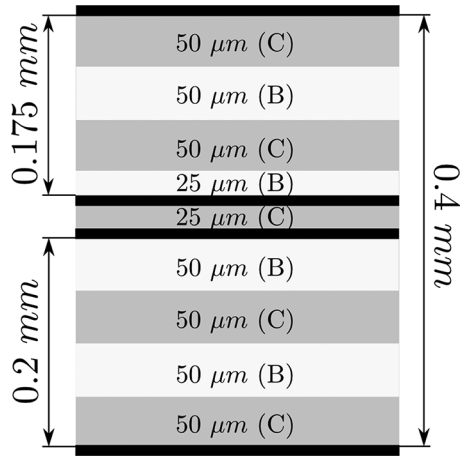

Fig. 10. Layer distribution (C: core film; B: bonding film).

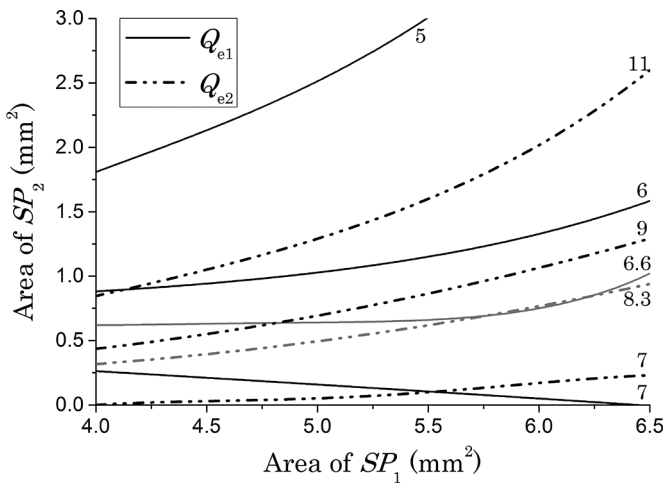

Fig. 11. Design I. I/O coupling (see Fig. 13 for resonator's dimensions). $h_c = 0.025$ mm, $h = 0.2$ mm, and $\epsilon_r = 3$.

A. Design I

The chosen center frequencies/FBW are 1.2 GHz/10% and 2.4 GHz/8%. As described in the previous section, in order to find the dimensions for the resonator, first L_{UIR} for 1.2 GHz is calculated from (7), which is 36.08 mm. From Figs. 4 and 3, the values $R_\theta = 3.4$ and $L_{\mathrm{MSIR}}/L_{\mathrm{UIR}} = 0.8$ are obtained, so $L_{\mathrm{MSIR}} = 28.86$. Finally, including $W_S = 0.2$ mm, the final length of the FMSIR is 14.63 mm. With the help of an EM simulator [22], the FMSIR has to be tuned to compensate for the effects of impedance steps and extra lengths in the lines (Δ_L), with L_T changing to 14.35 mm and R_θ to 3.2. Furthermore, in order to accommodate a patch for the common ground via, section A is reduced by 0.8 mm, forcing further modifications to the resonator.

From (8), the values $Q_{e1} = 6.6$ and $Q_{e2} = 8.3$ are obtained. Following the discussion from the previous section, from Fig. 11, the point where the curve $Q_{e1} = 6.6$ crosses $Q_{e2} = 8.3$ shows the required values for SP_1 and SP_2: 6 mm^2 and 0.7 mm^2, respectively, with $h_c = 0.025$ mm. As previously discussed, the inclusion of this two patches modifies the resonant frequencies, as well as the use of a common ground via, so at this stage, the dimensions of the resonator have to be adjusted to

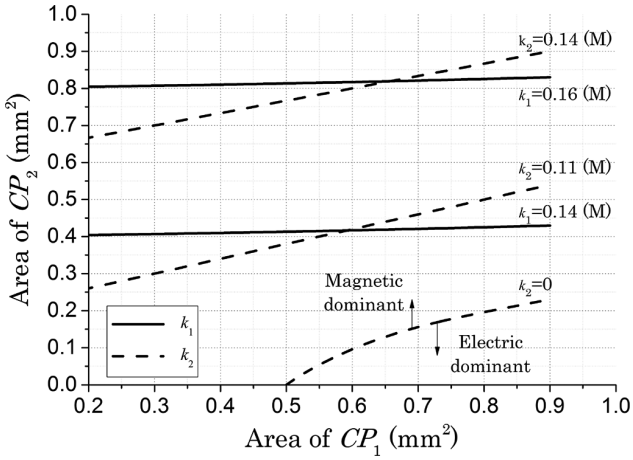

Fig. 12. Design I. Constant values of coupling coefficient depending on the area of CP_1 and CP_2. (M) Magnetic dominant mode (see Fig. 13 for resonator's dimensions). $h_c = 0.025$ mm, $h = 0.2$ mm, and $\epsilon_r = 3$.

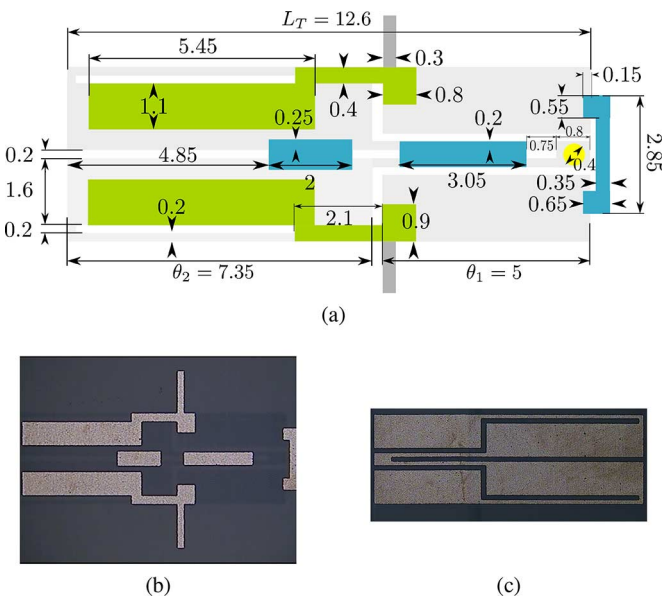

Fig. 13. Design I. (a) Dimensions summary (in mm). (b) Top-view photograph of the etched middle layer. (c) Etched resonator (bottom view of the middle layer).

compensate this effect and match the desired center frequencies, which are 1.2 and 2.4 GHz in this case. The final value for L_T is set to 12.6 mm and R_θ, to 1.47 (ignoring the length reduction in line section A to include the grounding via patch).

Regarding k, from (9) the values $k_1 = 0.136$ and $k_2 = 0.109$ are calculated. As in the previous step, the dimensions of CP_1 and CP_2 can be obtained from Fig. 12, being the point where both curves cut each other, i.e., $CP_1 = 0.6$ mm^2 and $CP_2 = 0.4$ mm^2.

Once the sizes for the resonators and patches are fixed, the stopband can be expanded by moving the coupling patches along the symmetry plane. As the structure is so compact, additional coupling paths are generated, producing additional transmission zeros. However, the values for the coupling patches would require further tuning. The completed design and dimensions are shown in Fig. 13. Furthermore, the physical

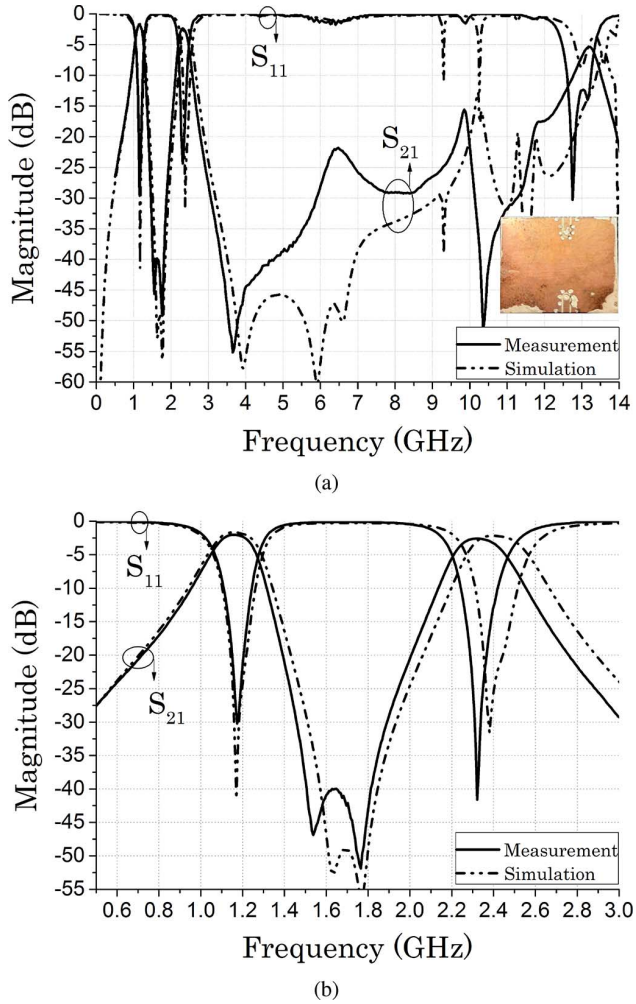

Fig. 14. Design I. Scattering parameters. Simulation versus. measurements. Fabricated device. (a) Wideband response. (b) Passband detail.

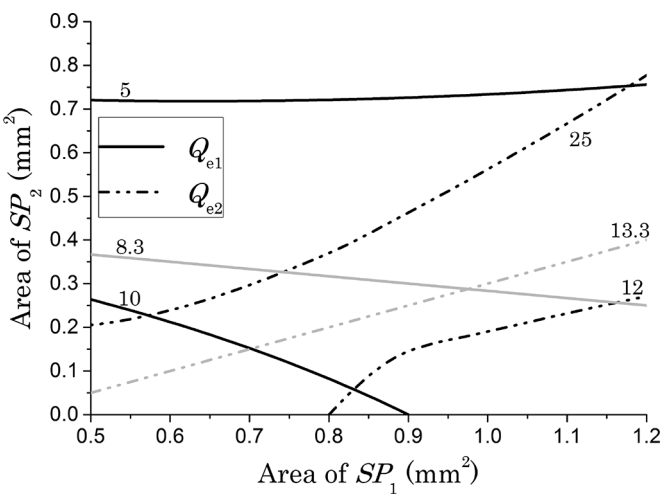

Fig. 15. Design II. I/O coupling (see Fig. 17 for resonator's dimensions). $h_c = 0.025$ mm, $h = 0.2$ mm, and $\epsilon_r = 3$.

realization for C_{TZ} (see Sections II-B and II-C) for splitting the inter-band TZ is also shown.

Results (Fig. 14) show good agreement between the simulated and measured results. It is demonstrated how the in-band

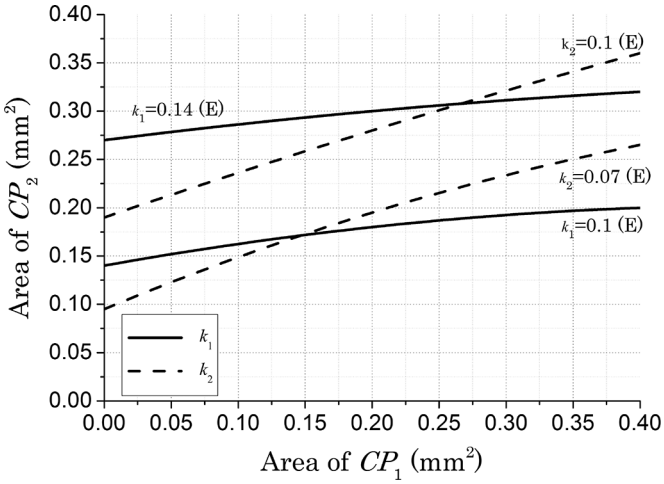

Fig. 16. Design II. Constant values of coupling coefficient depending on the area of CP_1 and CP_2. (M) Magnetic dominant mode (see Fig. 17 for resonator's dimensions). $h_c = 0.025$ mm, $h = 0.2$ mm, $\epsilon_r = 3$.

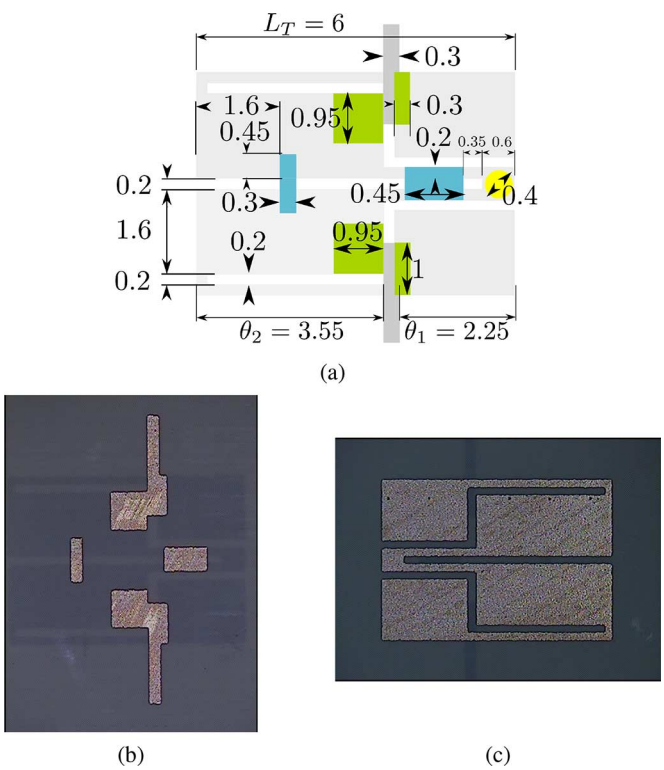

Fig. 17. Design II. (a) Dimensions summary (in mm) (b) Top-view photograph of the etched middle layer. (c) Etched resonator (bottom view of the middle layer).

second-order TZ splits into two TZ, with a separation proportional to the capacitance C_{TZ}. A slight shift in the second band's center frequency can be appreciated, due to small over-compression of the 25 μm core-film layer.

The prototype has been manufactured in LCP substrate with a dielectric constant of 3, following a standard fabrication process. The layer distribution is shown in Fig. 10. Results obtained show a very good agreement with the simulations (Fig. 14) on a compact design of $15.8 \times 10.2 \times 0.4$ mm^3, packaging included.

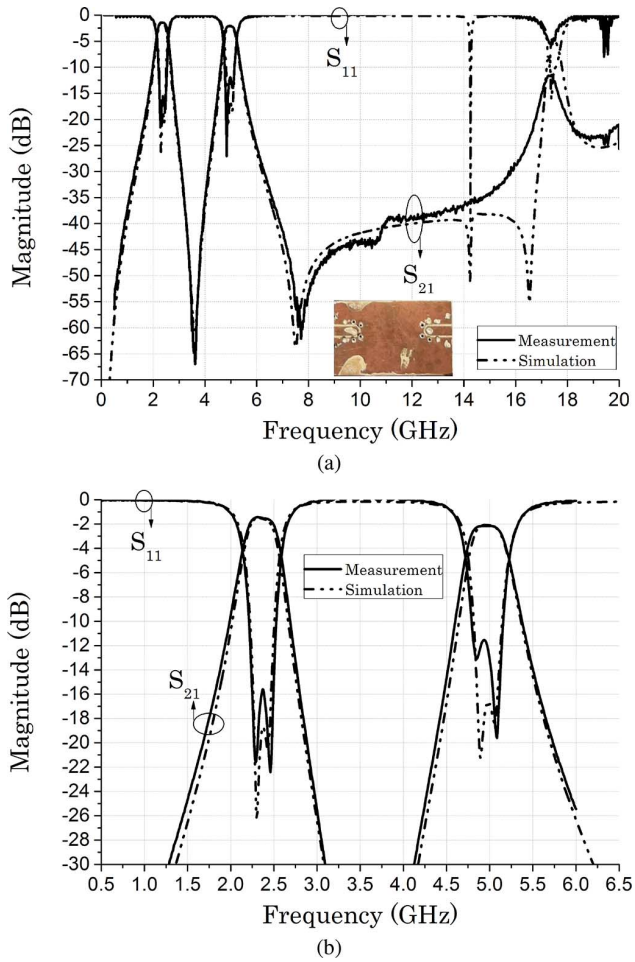

Fig. 18. Design II. Scattering parameters. Simulation versus. measurements. Fabricated device. (a) Wideband response. (b) Passband details.

B. Design II

The same design routine as in the previous section is followed, in this case aiming at 2.4/5 GHz WiFi bands with FBW's of 8% and 5%, maintaining the same layer distribution and R_Z. In this case, L_T and R_θ are changed to 6 mm and 1.57, respectively, and the width for the ground via patch is 0.6 mm.

Required values for Q_{e1} and Q_{e2} are 8.3 and 13.3 from (8), corresponding to SP_1 and SP_2 calculated as 0.95 and 0.3 mm^2 (Fig. 15). Regarding the coupling coefficient, required values of $k_1 = 0.109$ and $k_2 = 0.068$ correspond to $\mathrm{CP}_1 = 0.15$ mm^2 and $\mathrm{CP}_2 = 0.16$ mm^2. As discussed for the previous design, further improvement can be obtained for the stopband by adjusting the position of the patches, and eventually, their sizes. The final design has a footprint of $7.5 \times 11.2 \times 0.4$ mm^3, including the self-packaging. A summary of the dimensions is shown in Fig. 17 and the results in Fig. 18.

V. Conclusion

In this paper, a novel compact structure for designing self-packaged dual-band filters has been presented. This structure exhibits flexibility in terms of choosing the spacing between the bands by modifying the parameters of the two coupled dual-mode FMSIR. The coupling coefficient for each band can be

TABLE I
DUAL-BAND FILTERS COMPARISON

Ref.	Center freqs. (GHz)	FBW 1/2 (%)	IL (dB)	Size (λ_g^2)	Height (mm)	20 dB stop-band
[4]	2.45/5.5	8.1/21.8	1.5/1.2	0.02	0.76	N/A
[8]	1.2/3.5	Tunable	2.79/2.96	0.013	0.635	$9.84f_0$
[11]	2.45/5.2	11.4/11.3	2.2/1.1	0.0035	0.8	N/A
[12]	1.8/3.5	14/10	0.8/0.9	0.018	0.81	N/A
[15]	2.4/3.57	8.3/5.6	0.87/1.9	0.1	0.62	N/A
[16]	0.58/1.41	34.1/12.5	0.65/0.95	0.0078	1.27	N/A
This work (I)	1.2/2.4	10/8	1.79/2.37	0.0044	0.4	$8f_0$
This work (II)	2.4/5	8/5	1.42/2.16	0.006	0.4	$7f_0$

FBW=Fractional bandwidth; IL=Insertion loss;
f_0=Lower center frequency; λ_g=Guided wavelength at f_0

controlled independently by means of the areas of a pair of conductor patches over the resonators. Finally, the external quality factor is controlled by a second set of conductor patches. For the demonstration, two different designs have been presented. This type of packaged dual-band filter exhibits high rejection between the two passbands and a wide upper stopband. The validity of this approach has also been demonstrated by fabricating two prototypes. The results obtained show good agreement with the simulation results. Comparison to other reported filters is summarized in Table I.

ACKNOWLEDGMENT

The authors would like to thank Dr. N. Thomson, BSC Filters Ltd., for his support and encouragement throughout this research work.

REFERENCES

[1] X. Guan, Z. Ma, P. Cai, Y. Kobayashi, T. Anada, and G. Hagiwara, "Synthesis of dual-band bandpass filters using successive frequency transformations and circuit conversions," *IEEE Microw. Wireless Compon. Lett.*, vol. 16, no. 3, pp. 110–112, Mar. 2006.
[2] S. Fu, B. Wu, J. Chen, S. J. Sun, and C.-H. Liang, "Novel second-order dual-mode dual-band filters using capacitance loaded square loop resonator," *IEEE Trans. Microw. Theory Techn.*, vol. 60, no. 3, pp. 477–483, Mar. 2012.
[3] Y.-T. Kuo and C.-Y. Chang, "Analytical design of two-mode dual-band filters using e-shaped resonators," *IEEE Trans. Microw. Theory Techn.*, vol. 60, no. 2, pp. 250–260, Feb. 2012.
[4] J. Lee and Y. Lim, "A dual-band bandpass filter using dual and triple-mode resonators," in *Proc. IEEE Radio and Wireless Symp.*, Jan. 2012, pp. 143–146.
[5] L.-Y. Chen, C.-W. Tang, C.-T. Tseng, and Y.-C. Lin, "Design of planar dual-band bandpass filters with stepped-impedance resonators," in *Asia–Pacific Microw. Conf. Proc.*, Nov. 2013, pp. 521–523.
[6] A. Genc, R. Baktur, and R. Jost, "Dual-bandpass filters with individually controllable passbands," *IEEE Trans. Compon., Packag., Manuf. Technol.*, vol. 3, no. 1, pp. 105–112, Jan. 2013.
[7] C.-Y. Hsu, C.-Y. Chen, and H.-R. Chuang, "Microstrip dual-band bandpass filter design with closely specified passbands," *IEEE Trans. Microw. Theory Techn.*, vol. 61, no. 1, pp. 98–106, Jan. 2013.
[8] S.-C. Weng, K.-W. Hsu, and W.-H. Tu, "Compact and switchable dual-band bandpass filter with high selectivity and wide stopband," *Electron. Lett.*, vol. 49, no. 20, pp. 1275–1277, Sept. 2013.
[9] S.-C. Weng, K.-W. Hsu, and W.-H. Tu, "Independently switchable quad-band bandpass filter," *IET Microw. Antennas Propag.*, vol. 7, no. 14, pp. 1113–1119, Nov. 2013.
[10] R. Zhang, L. Zhu, and S. Luo, "Dual-mode dual-band bandpass filters with adjustable frequency ratio using an annular ring resonator," *IEEE Microw. Wireless Compon. Lett.*, vol. 23, no. 1, pp. 13–15, Jan. 2013.
[11] X. Dai, X. Y. Zhang, and Z. Y. Cai, "Compact ltcc dual-band bandpass filter using stepped impedance resonators," in *Proc. Cross Strait Quad-Regional Radio Science and Wireless Techn. Conf.*, Jul. 2013, pp. 109–112.
[12] L. Gao and X. Y. Zhang, "High-selectivity dual-band bandpass filter using a quad-mode resonator with source-load coupling," *IEEE Microw. Wireless Compon. Lett.*, vol. 23, no. 9, pp. 474–476, Sep. 2013.
[13] H. H. Ta and A.-V. Pham, "Dual band band-pass filter with wide stopband on multilayer organic substrate," *IEEE Microw. Wireless Compon. Lett.*, vol. 23, no. 4, pp. 193–195, Apr. 2013.
[14] G. Chaudhary, Y. Jeong, and J. Lim, "Dual-band bandpass filter with independently tunable center frequencies and bandwidths," *IEEE Trans. Microw. Theory Techn.*, vol. 61, no. 1, pp. 107–116, Jan. 2013.
[15] Y.-H. Cho and S.-W. Yun, "Design of balanced dual-band bandpass filters using asymmetrical coupled lines," *IEEE Trans. Microw. Theory Techn.*, vol. 61, no. 8, pp. 2814–2820, Aug. 2013.
[16] R. Zhang and L. Zhu, "Synthesis of dual-wideband bandpass filters with source-load coupling network," *IEEE Trans. Microw. Theory Techn.*, vol. 62, no. 3, pp. 441–449, Mar. 2014.
[17] M. Sagawa, M. Makimoto, and S. Yamashita, "Geometrical structures and fundamental characteristics of microwave stepped-impedance resonators," *IEEE Trans. Microw. Theory Techn.*, vol. 45, no. 7, pp. 1078–1085, July 1997.
[18] J.-S. Hong, *Microstrip Filters for RF/Microwave Applications*, 2nd ed. Hoboken, NJ, USA: Wiley, 2011.
[19] Q.-X. Chu and H. Wang, "A compact open-loop filter with mixed electric and magnetic coupling," *IEEE Trans. Microw. Theory Techn.*, vol. 56, no. 2, pp. 431–439, Feb 2008.
[20] J.-S. Hong and M. Lancaster, "Couplings of microstrip square open-loop resonators for cross-coupled planar microwave filters," *IEEE Trans. Microw. Theory Techn.*, vol. 44, no. 11, pp. 2099–2109, Nov. 1996.
[21] F. Cervera, J. Hong, and N. Thomson, "Development of packaged UWB passive devices using LCP multilayer circuit technology," in *Proc. 7th Eur. Microw. Integr. Circuits Conf.*, Oct. 2012, pp. 770–773.
[22] Sonnet Software Inc., EM User's Manual 2009.

Francisco J. Cervera (M'14) received the B.Eng. degree in telecommunications engineering from Universidad Europea de Madrid, Madrid, Spain, in 2007, and the M.Sc. degree in mobile communications from Heriot-Watt University, Edinburgh, U.K., where he is currently working toward the Ph.D. degree.

His research interests include miniature, self-packaged, multilayer RF/microwave filters using LCP materials, and integration for wireless communication and radar systems.

Jiasheng Hong (F'12), photograph and biography not available at the time of publication.